Hindawi
Journal of Applied Mathematics
Volume 2024, Article ID 5730530, 14 pages
https://doi.org/10.1155/2024/5730530

Research Article

Importance of Activation Energy on Magnetized Dissipative Casson-Maxwell Fluid through Porous Medium Incorporating Chemical Reaction, Joule Heating, and Soret Effects: Numerical Study

Nesreen Althobaiti

Department of Mathematics and Statistics, College of Science, Taif University, P.O. Box 11099, Taif 21944, Saudi Arabia

Correspondence should be addressed to Nesreen Althobaiti; nalthobaiti@gmail.com

Received 2 August 2023; Revised 6 December 2023; Accepted 14 December 2023; Published 5 January 2024

Academic Editor: Oluwole D. Makinde

In recent decades, the study of non-Newtonian fluids has attracted the interest of numerous researchers. Their study is encouraged by the significance of these fluids in fields including industrial implementations. Furthermore, the importance of heat and mass transfer is greatly increased by a variety of scientific and engineering processes, including air conditioning, crop damage, refrigeration, equipment power collectors, and heat exchangers. The key objective of this work is to use the mathematical representation of a chemically reactive Casson-Maxwell fluid over a stretched sheet circumstance. Arrhenius activation energy and aspects of the magnetic field also have a role. In addition, the consequences of both viscous dissipation, Joule heating, and nonlinear thermal radiation are considered. The method transforms partial differential equations originating in fluidic systems into nonlinear differential equation systems with the proper degree of similarity which is subsequently resolved utilizing the Lobatto IIIA technique's powerful computing capabilities. It is important to recall that the velocity profile drops as the Maxwell fluid parameter increases. Additionally, the increase in the temperature ratio parameter raises both the fluid's temperature and the corresponding thickness of the boundary layer.

1. Introduction

When describing fluid flow with viscosity that is dependent on shear, the power-law model is commonly employed. However, one cannot predict the consequences of flexibility. Fluids of either the second or third grade can exhibit the properties of elasticity. However, the viscosity does not become shear dependent with these sculptures. Additionally, they are unable to assess the outcomes of stress reduction. The Maxwell model, a class of fluids that has gained prominence, can be used to predict stress relaxation. Similar to the Maxwell model, a strictly elastic spring and strictly viscous damper might be expressed. The simulations of Maxwell nanofluid flow have attracted the interest for numerous scientists. The fractional model and the unstable nonlinear Cattaneo-Friedrich Maxwell (CFM) model were studied by Saqib et al. [1]. The fractional model is constructed from the fractional constitutive equations. Bayones et al. [2] looked upon the magnetic dissipative Soret of the continuous 2D Maxwell fluid flow across a stretching sheet involving Joule heating and chemical reaction inside a porous media. Plenty of research may be found in [3–12].

Due to the growing number of industrial applications and developing technology, non-Newtonian models of fluid flows have attracted more scholarly interest in recent years. Understanding of fluid dynamics and heat transmission requires a detailed study of the non-Newtonian fluid flow field at a boundary layer close to a stretched sheet. Numerous modern hypotheses have benefited from the research on non-Newtonian fluids. The Casson fluid is a non-Newtonian fluid with particular characteristics. The viscoelastic liquid model was initially presented by Casson in 1995. This model can now predict high shear-rate viscosity even in the absence of low and intermediate shear-rate data, which is useful for fuel engineers who evaluate sticky slurries. Kumar et al. [13] studied Casson nanofluid flow on a curved sheet. The stretching cylinder was used by Tamoor et al. [14] to present how the magnetic field impacted the flow of the Casson fluid. To distinguish the various components of heat transmission, they also used viscous dissipation and Joule-heating conditions. The references mention a number of additional works that discuss the Casson fluid model [15–17].

In recent years, non-Newtonian fluid flows have gained attention due to their significance in many industrial and technical operations. But their rheological characteristics are so diverse that it is not possible to analyse their behavior with a single constitutive correlation. As a result, many fluid models have been created to accurately characterise the properties of non-Newtonian materials. In a parabolic trough solar collector, Casson-Maxwell, Casson-Jeffrey, and Casson-Oldroyd-B binary nanofluids were compared with engine oil by Raafat and Ibrahim [18]. With the appropriate similarity variables, the partial differential equations controlling the flow of nanofluids were converted into ordinary differential equations to solve the model. The MHD boundary layer with numerous slip conditions on the Williamson and Maxwell nanofluid over a stretched sheet soaked in a porous medium was discussed by Kanimozhi et al. [19]. For the velocity and temperature profiles with and without suction, a dual solution was carried out. Gangadhar et al. [20] investigated the viscoelastic properties of an axisymmetric Casson-Maxwell nanoliquid flow across two stationary discs. Many studies have addressed the intricate non-Newtonian properties of Casson-Maxwell models; they can be found in [21, 22]. Furthermore, other investigations have been identified [23–28].

The activation energy of a chemical reaction, or the minimum amount of energy required to initiate an activity, is indirectly correlated with the reaction's rate (such as a chemical reaction). Using an adapted Buongiorno model, Jyothi et al. [29] examined how activation energy affected the dynamics of Casson hybrid nanofluid flow across an upward/downward rotating disc. Kumar et al. [30] have considered concurrently single-multiwalled CNTs to investigate the impacts of a micropolar nanofluid. The importance of activation energy in the Maxwell fluid flow across a stretching cylinder was examined by Sowmiya and Kumar [31]. The results showed that as the heat generation/absorption parameter values raised, the temperature and the related boundary layer thickness decreased. Moreover, raising the radiation parameter raises the fluid's temperature, whereas raising the activation energy parameter raises the concentration boundary layer's thickness. It is feasible to examine more noteworthy studies on activation energy in various settings [32, 33].

Magnetohydrodynamic (MHD) fluxes are necessary for the construction of nuclear reactors as well as other technological and industrial applications. The mobility of electrically conducting materials in a magnetic field is studied using MHD. Several novel and anticipated researches have shown how the presence of a magnetic field significantly alters the transport characteristics and heat transfer of typical electrically conducting flows. Khan et al. [34] argued for a time-dependent Casson fluid over a stretched surface utilizing a magnetic field, mass suction, and a nonuniform heat source. Moreover, Dar [35] investigated the effects of thermal radiation, heat source/sink, and thermal slip on blood peristaltic flow caused by magnetic field alignment. Mohana and Kumar [36] examined how radiation, a heat source, and Joule-heating effects affected the form of the copper-water nanofluid on MHD boundary layer flow and heat transfer across a nonlinear stretched sheet in a porous media. The bvp4c solver that comes with MATLAB is used to compute the numerical solutions. Moreover, Padmaja et al. [37] investigated a chemically reactive $Cu–H_20$ on MHD nanofluid swirl coating flow on a rotating vertical electrically insulated cone next to a porous medium in the presence of a radial static magnetic field. Several studies are also found in [38, 39].

Porous media is a practical way to manage heat transfer and control fluid velocity in a variety of manufacturing applications, such as radioactive waste disposal and oil extraction. While a modified Darcy-Forchheimer model is utilized to formulate problems involving high-speed flow, the characteristics of this material are still explained by the classical Darcy rule. In cell technologies, drying procedures, extraction of oils, material processing, etc., porous media flows are highly concentrated. In order to describe the three-dimensional flow of nanofluid in a porous medium, Muhammad et al. [40] discussed the Darcy-Forchheimer formula. Hassan et al. [41] investigated convective heat transport in a porous material through a wave-like surface using the Dupuit-Forchheimer model. The Darcy-Brinkman-Forchheimer equation was used by Bhatti et al. [42] to study the mathematical modelling of a two-phase fluid flow model across a porous material in the presence of an external magnetic field. Additionally, Padmaja and Kumar [43] demonstrated the numerical analysis of a nanofluid moving at a constant speed via a vertical plate in a porous media under Dufour and Soret effects in conjunction with a higher order chemical reaction. See [44–48] for a list of further recent studies conducted in this topic.

This work is aimed at analysing the complex model of two non-Newtonian models and determining the factors that improve the efficiency of the device. Additionally, we want to find novel characteristics of activation energy in the Casson-Maxwell fluid under the influence of Joule heating, viscous dissipation, and nonlinear thermal radiation circumstances across a stretched permeable sheet. For binary chemical reactions, the modified Arrhenius activation energy formula is applied. The mathematical model is deciphered using the MATLAB programme by utilizing Lobatto IIIA technique [49, 50]. To investigate how significant variables affect the properties of fluids, tables and graphs are employed. The work's novel outcomes further aid in determining performance in non-Newtonian fluid models and significantly reduce energy loss in thermal devices. By using the results of this work, thermal energy systems can be made more competent and efficient in many industrial, engineering, and biomedical fields in a cost-effective and ecologically friendly way.

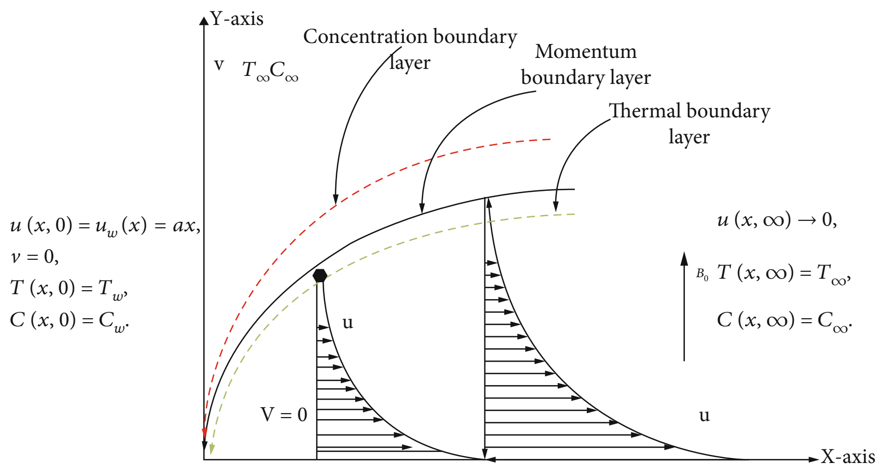

FIGURE 1: Schematic configuration.

2. Flow Model and Mathematical Formulation

Consider a two-dimensional incompressible Casson-Maxwell fluid model with an activation energy in the region $(y > 0)$ along a nonlinearly porous stretched sheet. This model is subject to the influence of a magnetic field, Joule heating, viscous dissipation, and chemical reaction. Figure 1 depicts the physical flow and coordinate system. With a fixed origin, the surface is stretched over the flow direction due to the action of equal and opposing forces. However, the sheet's stretching along the x-axis caused fluid flow to occur. It is further assumed that the stretching sheet's surface is kept at T_w and C_w. Additionally, it is expected that T_w and C_w are larger than T_∞ and C_∞, respectively.

The rheological equation below could be used to the Casson fluid (CF) as an isotropic, incompressible flow to [9]:

$$\tau_{ij} = \begin{cases} 2\left(\mu_B + \dfrac{P_y}{\sqrt{2\Pi}}\right)e_{ij}, & \Pi > \Pi_c, \\ 2\left(\mu_B + \dfrac{P_y}{\sqrt{2\Pi_c}}\right)e_{ij}, & \Pi < \Pi_c. \end{cases} \tag{1}$$

P_y represents the Casson fluid yield stress provided by

$$P_y = \frac{\mu_B\sqrt{(2\Pi)}}{\beta_3}. \tag{2}$$

When $\Pi > \Pi_c$ for the Casson fluid flow, then

$$\mu_0 = \mu_B + \frac{P_y}{\sqrt{(2\Pi)}}. \tag{3}$$

Thus, the Casson number, plastic dynamic viscosity, and fluid density all influence the kinematic viscosity; hence,

$$\mu_0 = \frac{\mu_B}{\rho}\left(1 + \frac{1}{\beta_3}\right). \tag{4}$$

The ordinary Newtonian fluid is favoured by the constitutive Eq. (4) when $\alpha \longrightarrow \infty$.

The one elastic parameter in the Maxwell model "λ" makes it a straightforward linear model. This model derives the following relationship by fusing the ideas of fluid viscosity and solid elasticity [9].

$$\tau + \lambda\frac{\partial \tau}{\partial y} = \mu_0\gamma. \tag{5}$$

The steady-state conditions guiding the flow model equations within a porous media are provided below with the aid of the aforementioned assumptions and boundary layer assumptions as follows [6, 9, 10]:

$$\frac{\partial u}{\partial x} + \frac{\partial v}{\partial y} = 0, \tag{6}$$

$$\begin{aligned} u\frac{\partial u}{\partial x} + v\frac{\partial v}{\partial y} = \nu\left(1+\frac{1}{\alpha}\right)\frac{\partial^2 u}{\partial y^2} \\ - \lambda\left[u^2\frac{\partial^2 u}{\partial x^2} + v^2\frac{\partial^2 u}{\partial y^2} + 2uv\frac{\partial^2 u}{\partial x \partial y}\right] \\ - \frac{\sigma B_0^2}{\rho}u - \frac{\nu}{k}u, \end{aligned} \tag{7}$$

$$u\frac{\partial T}{\partial x} + v\frac{\partial T}{\partial y} = \frac{K}{\rho c_p}\frac{\partial^2 T}{\partial y^2} + \frac{\mu}{\rho c_p}\left(\frac{\partial u}{\partial y}\right)^2 + \frac{\sigma B_0^2}{\rho}u^2 - \frac{1}{\rho c_p}\frac{\partial q_r}{\partial y}, \tag{8}$$

$$u\frac{\partial C}{\partial x} + v\frac{\partial C}{\partial y} = D_N\frac{\partial^2 C}{\partial y^2} - K_{r'}(C - C_\infty)\left(\frac{T}{T_\infty}\right)^m \exp\left[\frac{-E^*}{KT}\right] + \frac{D_N K_T}{T_m}\frac{\partial^2 T}{\partial y^2}. \tag{9}$$

The radiative flux for radiation q_r is designed using the Rosseland diffusion approximation and is given as [9, 35]

$$q_r = -\frac{\partial T^4}{\partial y}\frac{4\sigma^*}{3k^*}. \tag{10}$$

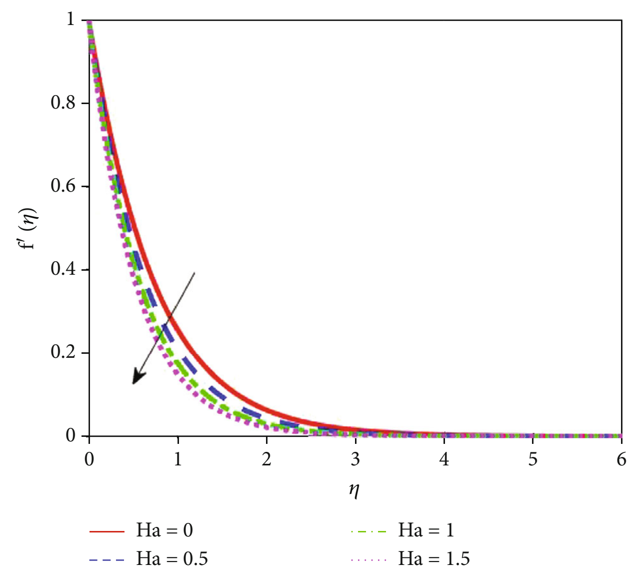

Figure 2: Effect of Ha on velocity function.

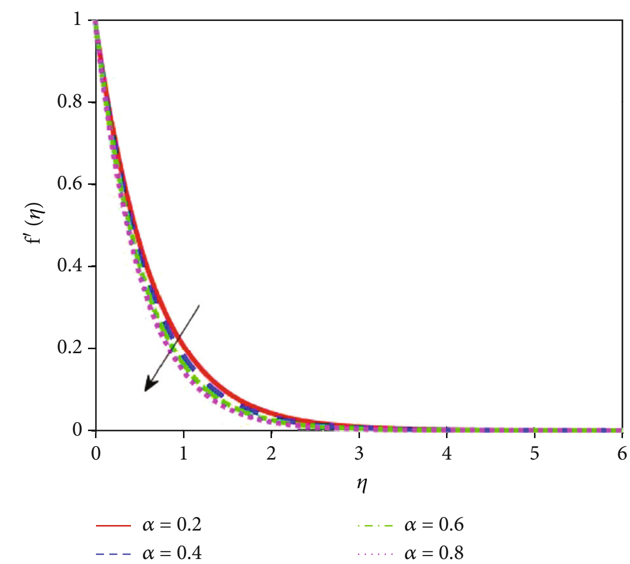

Figure 4: Effect of α on velocity function.

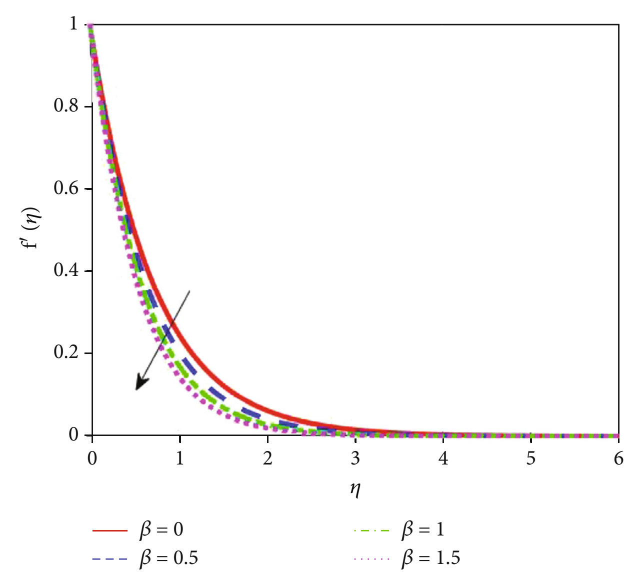

Figure 3: Effect of β on velocity function.

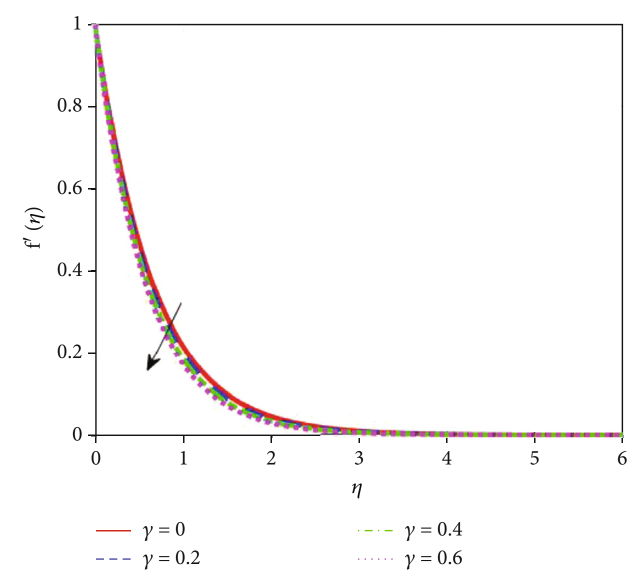

Figure 5: Effect of γ on velocity function.

It is crucial that this model considers the optically thick radiation limit, assuming that T^4 can be represented as the linear combination of temperatures and that the temperature variations within the flow are sufficiently modest. This is done by utilizing the Taylor series regarding T_0 and expanding T^4 as follows:

$$T^4 = T_0^4 + 4T_0^3(T - T_0) + 6T_0^2(T - T_0)^2 + \cdots. \tag{11}$$

We get the following result by ignoring the higher-order terms (second order onwards) in $(T - T_0)$:

$$T^4 \simeq 3T_0^4 + 4T_0^3 T. \tag{12}$$

Using Eq. (12) and differentiating Eq. (10) with regard to y, one can obtain

$$\frac{\partial q_r}{\partial y} = -\frac{16\sigma^* T_0^2}{3k^*}\frac{\partial T}{\partial y^2}. \tag{13}$$

The partial differential Eqs. (6)–(9) are governed by the following boundary conditions [5, 10]:

$$\begin{aligned} &u = ax, u_w(x) = ax, v = 0, T = T_w, C = C_w at y = 0, \\ &u \longrightarrow 0, T \longrightarrow T_\infty, C \longrightarrow C_\infty at y \longrightarrow \infty. \end{aligned} \tag{14}$$

The following list includes the similarity transformations which are employed to break down the system of these

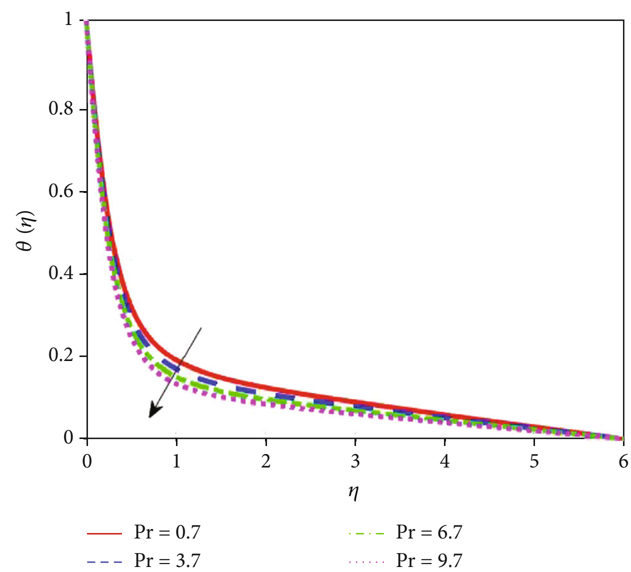

FIGURE 6: Effect of Pr on temperature function.

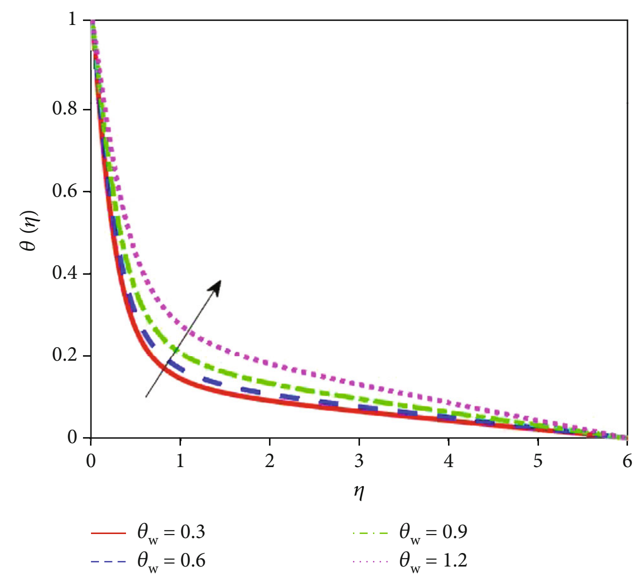

FIGURE 7: Effect of θ_w on temperature function.

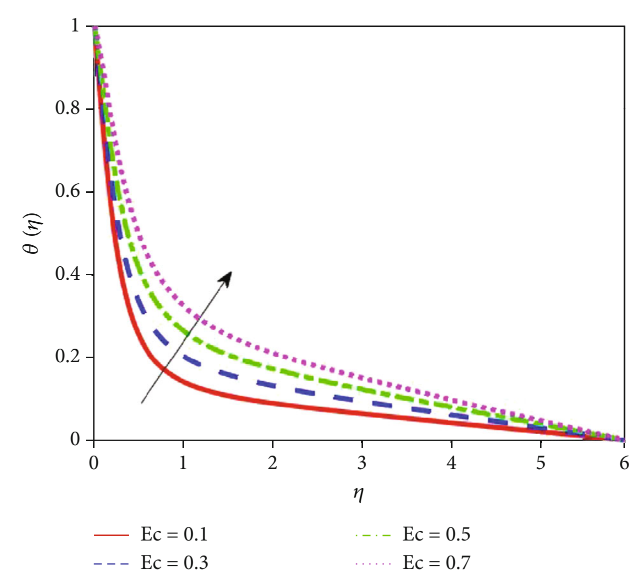

FIGURE 8: Effect of Ec on temperature function.

complex linked PDEs in the given issue into a collection of ordinary differential equations (ODEs) [5, 9, 10, 18]:

$$\begin{gathered} u = axf'(\eta), v = -\sqrt{av}f(\eta), \psi = \sqrt{av}xf(\eta), \\ \theta(\eta) = \frac{T - T_\infty}{T_w - T_\infty}, \phi(\eta) = \frac{C - C_\infty}{C_w - C_\infty}, \eta = \left(\frac{a}{v}\right)^{1/2} y. \end{gathered} \tag{15}$$

The following is a list of the dimensionless numbers employed in the guiding equations:

$$\begin{gathered} \mathrm{Ha} = \frac{\sigma B_0^{\,2}}{\rho a}, \gamma = \frac{\nu}{ak}, \Pr = \frac{\nu \rho c_p}{K}, \mathrm{Ec} = \frac{u_w^{\,2}}{c_p(T_w - T_\infty)}, \mathrm{Sc} = \frac{\upsilon}{D_N}, \\ \mathrm{Kr} = \frac{K_{r'}}{a}, \mathrm{Rd} = \frac{16\sigma^* T_0^{\,3}}{3k^* K}, E_1 = \frac{E^*}{KT_\infty}, \theta_w = \frac{T_w}{T\infty}, \beta = a\lambda, \\ \alpha = \left(\frac{P_y}{\mu_B \sqrt{2\pi_c}}\right)^{-1}, \mathrm{Sr} = \frac{(D_N K_T / \upsilon T_m) \times (T_w - T_\infty)}{(C_w - C_\infty)}. \end{gathered} \tag{16}$$

3. Solution of the Problem

Equation (14) is satisfied when the transformations that were previously mentioned (Eq. (15)) are applied using non-dimensional parameters (Eq.(16)). Simplifying the governing partial differential equations, Eqs. (7)–(9) yield

$$\left(1 + \frac{1}{\alpha}\right) f''' + ff'' - f'^2 - Mf' + \beta\left(2ff'f'' - f^2 f'''\right) - \gamma f' = 0, \tag{17}$$

$$\left(1 + \frac{4}{3}\mathrm{Rd}\right)\theta'' + \Pr\mathrm{Ec}\left[f''^2 + \mathrm{Ha}f'^2\right] + \Pr f\theta' + \frac{4}{3}\mathrm{Rd}\begin{bmatrix} (\theta_w - 1)^3\left(3\theta'^2\theta^2 + \theta^3\theta''\right) \\ +3(\theta_w - 1)\left(\theta'^2 + \theta\theta''\right) \\ +3(\theta_w - 1)^2\left(2\theta'^2\theta + \theta^2\theta''\right) \end{bmatrix} = 0, \tag{18}$$

$$\begin{gathered} \phi'' - \mathrm{ScKr}\phi((\theta_w - 1)\theta + 1)^m \exp\left(\frac{-E_1}{((\theta_w - 1)\theta + 1)}\right) \\ + \mathrm{SrSc}\theta'' + \mathrm{Sc}f\phi' = 0. \end{gathered} \tag{19}$$

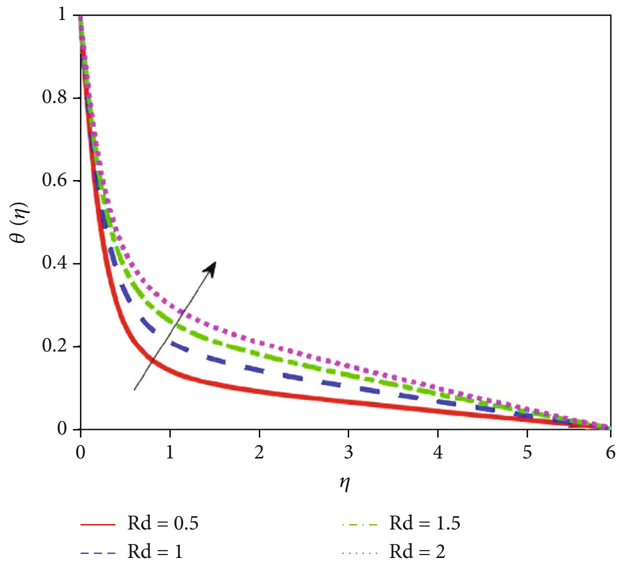

Figure 9: Effect of Rd on temperature function.

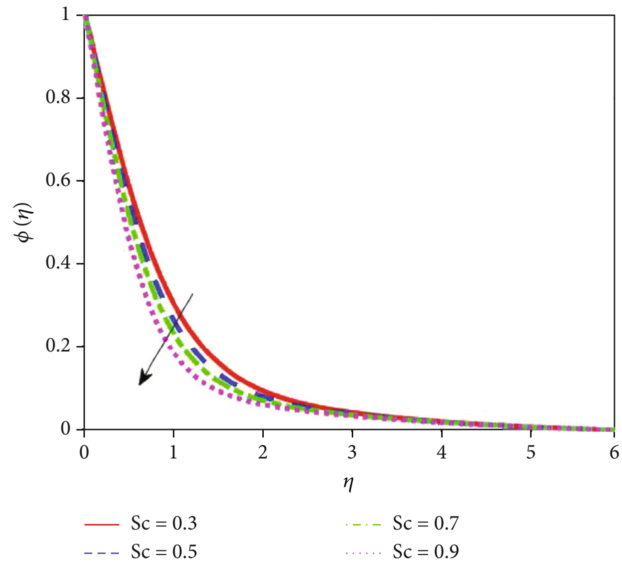

Figure 10: Effect of Sc on concentration function.

Moreover, the following are the regulating boundary conditions according to of Eq. (15) [5, 10]:

$$\begin{gathered} f(0)=0, f'(0)=1, \theta(0)=1, \phi(0)=1 at \eta=0, \\ f'(\infty) \longrightarrow 0 \theta(\infty) \longrightarrow 0 \phi(\infty) \longrightarrow 0 as \eta \longrightarrow \infty. \end{gathered} \tag{20}$$

The nondimensional local skin friction coefficient Cf_x, Nusselt number Nu_x, and Sherwood number Sh_x are given as follows [5, 10]:

$$\begin{aligned} \mathrm{Cf}_x &= \frac{\tau_w}{\rho {u_w}^2}, \\ \mathrm{Nu}_x &= \frac{x q_w}{K(T_w - T_\infty)}, \\ \mathrm{Sh}_x &= \frac{x q_m}{D_N (C_w - C_\infty)}. \end{aligned} \tag{21}$$

Here, τ_w represents the wall shear stress, q_w represents the heat flux, and q_m represents the mass flux, all of which are taken as follows:

$$\begin{aligned} \tau_w &= \mu \left(\frac{\partial u}{\partial y} \right)_{y=0}, \\ q_w &= -K \left(\frac{\partial T}{\partial y} \right)_{y=0}, \\ q_m &= -D_N \left(\frac{\partial C}{\partial y} \right)_{y=0}. \end{aligned} \tag{22}$$

Finally, the nondimensional equations of drag force and heat and mass transport rates are obtained, respectively, as follows [6]:

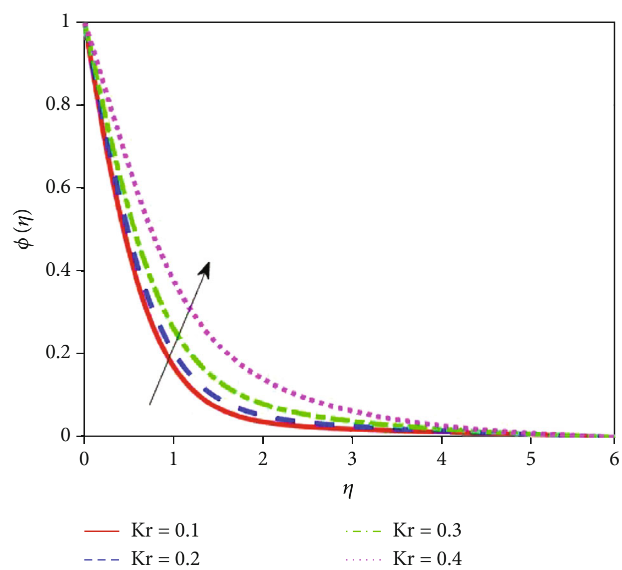

Figure 11: Effect of Kr on concentration function.

$$\begin{aligned} \mathrm{Cf}_x {\mathrm{Re}_x}^{0.5} &= f''(0), \\ \mathrm{Nu}_x {\mathrm{Re}_x}^{-0.5} &= -\left(1 + \frac{4}{3} (\theta_w - 1)\theta(0) + 1 \right)^3 \theta'(0), \\ \mathrm{Sh}_x {\mathrm{Re}_x}^{-0.5} &= -\phi'(0). \end{aligned} \tag{23}$$

Here, $\mathrm{Re}_x = a x^2 / v$ is the local Reynolds number.

4. Computational Procedure

The system of complex coupled PDEs that govern the physical issue under consideration is reduced to the system of ODEs with the help of the proper similarity transformations. Additionally, the "bvp4c" function built in is used to streamline the reduced system of nonlinear (ODEs) Eqs. (17)–(19).

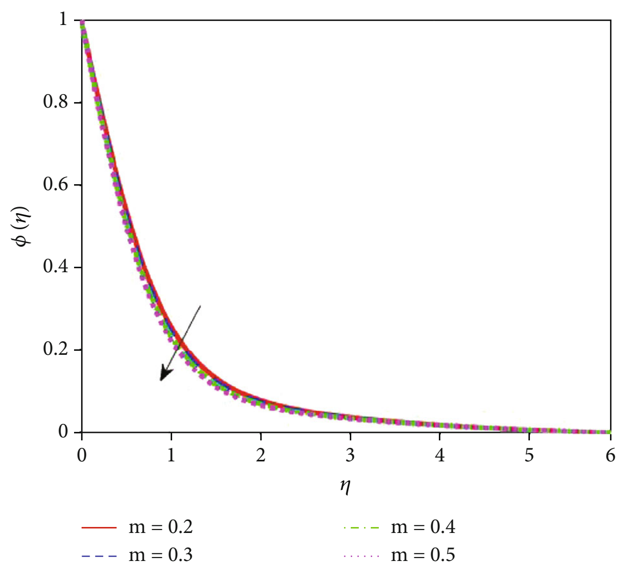

Figure 12: Effect of m on concentration function.

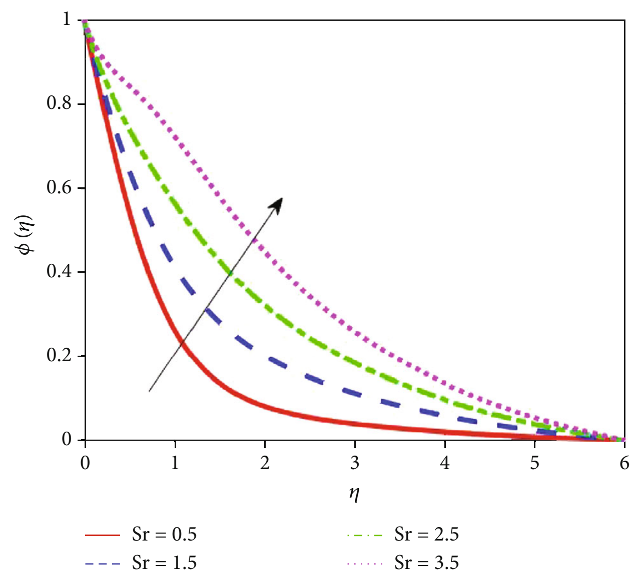

Figure 13: Effect of Sr on concentration function.

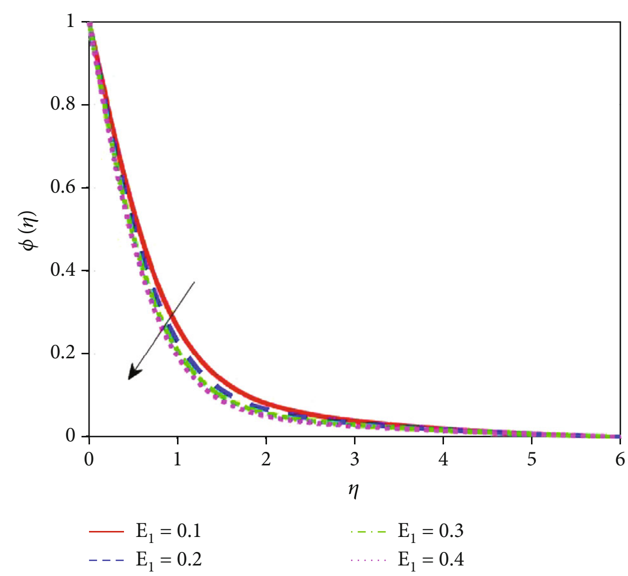

Figure 14: Effect of E_1 on concentration function.

In order to achieve this, first-order ODEs are created from the combination of Eqs. (17)–(19) (ODEs), which can be summed up as follows:

$$\begin{aligned}
\xi_1' &= \xi_2,\\
\xi_2' &= \xi_3,\\
\xi_3' &= \frac{(\xi_2)^2 + \gamma_1\xi_2 + Ha\xi_2 - \xi_1\xi_3 - 2\beta\xi_1\xi_2\xi_3}{(1/(1+\alpha)) - \beta(\xi_1)^2},\\
\xi_4' &= \xi_5,\\
\xi_5' &= \frac{-4/3}{1 + 4/3Rd\left[(1-\theta_w)^3(\xi_4)^3 + 3(1-\theta_w)^2(\xi_4)^2 + 3(1-\theta_w)\xi_4\right]}[\chi],\\
\xi_6' &= \xi_7,\\
\xi_7' &= \mathrm{ScKr}\xi_6((\theta_w-1)\xi_4+1)^m \exp\left(\frac{-E_1}{((\theta_w-1)\xi_4+1)}\right) - \mathrm{Sc}\xi_1\xi_7 - \mathrm{SrSc}\xi_5',
\end{aligned} \tag{24}$$

where $\chi = [3(1-\theta_w)^3(\xi_5)^2(\xi_4)^2 + 6(1-\theta_w)^2(\xi_5)^2\xi_4 + 3(1-\theta_w)(\xi_5)^2] - \mathrm{Pr}\xi_1\xi_5 - \mathrm{PrEc}[(\xi_3)^2 + Ha(\xi_2)^2]$.

The boundary conditions are

$$\begin{aligned}
&\xi_1(0) = 0, \xi_2(0) = 1, \xi_4(0) = 1, \xi_6(0) = 1,\\
&\xi_2(\infty) = 0, \xi_4(\infty) = 0, \xi_6(\infty) = 0,
\end{aligned} \tag{25}$$

where

$$\begin{aligned}
&\xi_1 = f, \xi_2 = \xi_1' = f', \xi_3 = \xi_2' = f'',\\
&\xi_4 = \theta, \xi_5 = \xi_4' = \theta'\xi'_5 = \theta'',\\
&\xi_6 = \phi, \xi_7 = \xi_6' = \phi'\xi_7' = \phi''.
\end{aligned} \tag{26}$$

5. Findings and Discussion

Figures 2–16 detail the impact of various particular characteristics on velocity $f'(\eta)$ in the direction x-axis, temperature $\theta(\eta)$, and concentration $\phi(\eta)$. The momentum, energy, and concentration equations, along with the proper boundary conditions, are the core components of the set of highly nonlinear correlated partial differential equations that regulate the current mathematical representation of the physical issue. An assortment of nonlinear coupled ordinary differential equations is obtained using the right similarity modifications, and a reliable numerical method is used with the help of the MATLAB function "bvp4c." Physical quantities that are valuable to engineers, and local skin friction coefficients, local Nusselt number, and local Sherwood number are also illustrated and shown in graphical and tabular configurations. The implications on velocity, temperature, and concentration are caused by specific flow-controlling parameters, and they are displayed in conjunction with these

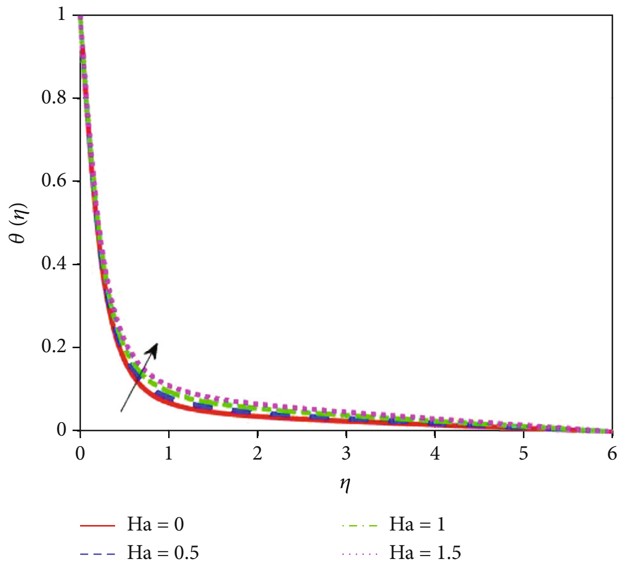

Figures 15: Effect of Ha on temperature function.

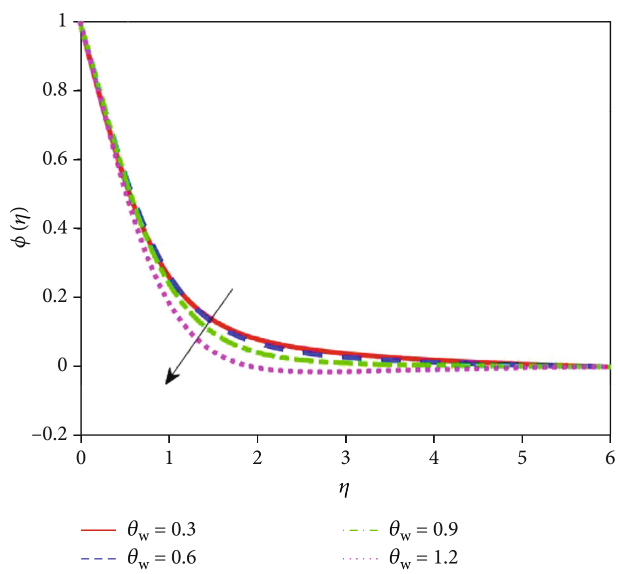

Figure 16: Effect of θ_w on concentration function.

effects. The following referred tables display fifteen possibilities. Different values are assigned to various variables in these tables depending on the circumstances. To show the fluctuation of each parameter, we have this 15 scenarios. Numerical calculations demonstrate the sufficient accuracy and improved convergence attained by the computing scheme. The maximum residual error (MRE) found throughout the numerical computation process is shown in Table 1 and demonstrates the convergence and accuracy of the suggested method. According to the greatest residual acquired for several cases of each scenario during problem evaluation, Table 1 shows halting criteria. The computer simulation values of mesh points determined for variations of tolerance for each fluidic parameter are displayed in Table 2 according to the proposed scheme. That is, Table 2 lists the mesh points utilized to solve each of the fifteen

Table 1: Magnitude of relative errors for different cases.

Scenarios	Case 1	Case 2	Case 3	Case 4
1	3.82065627 678433*e*-11	1.80874757 119233*e*-11	8.89830167 583457*e*-11	4.34521191 577676*e*-10
2	4.79669789 068006*e*-11	1.80874757 119233*e*-11	2.50414662 234981*e*-11	4.71638985 217215*e*-11
3	1.8087475 7119233*e*-11	2.17957108 676383*e*-11	2.926256547 34630*e*-11	3.20510777 777123*e*-11
4	1.54688355 497429*e*-11	1.98252710 792465*e*-11	3.18575784 474851*e*-10	8.89668758 526627*e*-11
5	1.80874757 119233*e*-11	1.93528342 053979*e*-11	3.99968496 794806*e*-11	1.72908981 866510*e*-10
6	1.80874757 119233*e*-11	1.93528342 053979*e*-11	3.99968496 794806*e*-11	1.72908981 866510*e*-10
7	1.80874757 119233*e*-11	1.8043244 9248245*e*-11	2.20101565 323902*e*-11	4.1639693 4617898*e*-11
8	1.80874757 119233*e*-11	5.74079595 580194*e*-12	6.07242785 763480*e*-12	6.70837002 256024*e*-12
9	1.80874757 119233*e*-11	1.81066181 051757*e*-11	1.812471582 88821*e*-11	1.8142228 4189586*e*-11
10	1.80740949 273034*e*-11	1.80874757 119233*e*-11	1.6914881 3741183*e*-11	5.621639 20786861*e*-12
11	1.6873739 0452115*e*-11	1.80802786 328972*e*-11	1.80874757 119233*e*-11	1.80987054 120189*e*-11
12	1.80874757 119233*e*-11	1.591419854 05877*e*-11	1.51907058 116046*e*-11	1.3851350 2997190*e*-11
13	1.80874757 119233*e*-11	1.80814583 321136*e*-11	1.80779854 244237*e*-11	1.8075902 1069288*e*-11
14	3.8206562 7678433*e*-11	1.808747571 19233*e*-11	8.89830167 583457*e*-11	4.345211 91577676*e*-10
15	1.8087475 7119233*e*-11	1.80432449 248245*e*-11	2.20101565 323902*e*-11	4.163969 34617898*e*-11

Table 2: Data for the number of meshes for various cases.

Scenarios	Case 1	Case 2	Case 3	Case 4
1	1072	880	980	793
2	796	880	965	996
3	880	861	847	823
4	877	870	795	977
5	880	894	898	898
6	880	894	898	898
7	880	870	865	846
8	880	896	899	899
9	880	877	874	872
10	828	880	893	898
11	836	873	880	878
12	880	885	890	894
13	880	880	878	876
14	1072	880	980	793
15	880	870	865	846

Table 3: Numerical data of skin friction (Cf_x).

Scenarios	Case 1	Case 2	Case 3	Case 4
1	-1.28077681773403	-1.49481990621989	-1.68262952737397	-1.85180542896513
2	-1.38564826527106	-1.49481990621989	-1.59855718351559	-1.69718214883318
3	-1.49481990621989	-1.61458900911085	-1.72606789007474	-1.83077132551753
4	-1.45443250476163	-1.53417606280295	-1.61007721180059	-1.68262952736751
5	-1.49481990621989	-1.49481990625349	-1.49481990627297	-1.49481990627009
6	-1.49481990621989	-1.49481990621989	-1.49481990618858	-1.49481990600592
7	-1.49481990621989	-1.49481990628338	-1.49481990628338	-1.49481990628338
8	-1.49481990621989	-1.49481990621989	-1.49481990621989	-1.49481990621989
9	-1.49481990621989	-1.49481990621989	-1.49481990624284	-1.49481990628338
10	-1.49481990622875	-1.49481990621989	-1.49481990621989	-1.49481990622422
11	-1.49481990621989	-1.49481990621989	-1.49481990621989	-1.49481990621989
12	-1.49481990621989	-1.49481990623692	-1.49481990624447	-1.49481990625786
13	-1.49481990621989	-1.49481990621989	-1.49481990621989	-1.49481990621989
14	-1.28077681773403	-1.49481990621989	-1.68262952737397	-1.85180542896513
15	-1.49481990621989	-1.49481990621989	-1.49481990618858	-1.49481990600592

Table 4: Discrepancy of the rate of heat transfer $[-(1+(4/3)(\theta_w-1)\theta(0)+1)^3]$.

Scenarios	Case 1	Case 2	Case 3	Case 4
1	0.345985470462596	0.294945767860730	0.254974136194463	0.221709862075500
2	0.315805421515249	0.294945767860730	0.277946931999264	0.263464790215048
3	0.294945767860730	0.281307233769240	0.269458945285795	0.258900236044544
4	0.299383260112508	0.290719013999120	0.282812961429017	0.275523088611018
5	0.294945767860730	-0.0675738089505146	-0.396829454530563	-0.660866283211299
6	0.294945767860730	-0.0675738089505146	-0.396829454530563	-0.660866283211299
7	0.294945767860730	0.302141979360025	0.304823853378090	0.300565837887552
8	0.294945767860730	0.0297142438661200	-0.236529188719365	-0.503643752060890
9	0.294945767860730	0.316807363093821	0.335474538943090	0.351852272402975
10	0.294945767860730	0.294945767860730	0.294945767864266	0.294945767869380
11	0.294945767861448	0.294945767860729	0.294945767860730	0.294945767861675
12	0.294945767860730	0.294945767862217	0.294945767863027	0.294945767864747
13	0.294945767860730	0.294945767860730	0.294945767860730	0.294945767860729
14	0.345985470462596	0.294945767860730	0.254974136194463	0.221709862075500
15	0.294945767860730	0.302141979360025	0.304823853378090	0.300565837887552

cases. For various changes in all cases, Tables 3–5 give the skin friction, Nusselt number, and Sherwood number variations, respectively, for adjusted values of all relevant physical parameters. Table 6 presents a comparison between the presented results and those reported by Palaiah et al. [10] of C $f_x\mathrm{Re}_x^{0.5}$ and $\mathrm{Cf}_x\mathrm{Nu}_x^{0.5}$ for different values of the Ha, Ec, Pr, Sr, Sc, and Kr in the absence of$\alpha = \infty = 0$ and$\gamma = Rd = m = E_1 = 0$effects. They are in extremely excellent agreement with one another. As exhibited in Table 6, the current results serve as a benchmark for the precision of our numerical procedures.

Figure 2 illustrates how the magnetic parameter Ha affects the velocity distribution, which gradually decreases within the boundary layer as the magnetic parameter increases in the x-direction. The induced magnetic field causes a resistance force termed as the Lorentz force in an electrically conductive fluid that slows the velocity of the Casson-Maxwell fluid inside the boundary layer. On a physical level, this is caused by how the magnetic and electric fields are affected by the motion of an electrically conducting fluid. A resistance force develops in the fluid flow when a magnetic field is present. By applying this force, the fluid's velocity may be slowed. It has been noted that the current work and the work done by [5, 10] are in good agreement. As can be seen in Figure 3, the elevated Maxwell fluid variable β reduces the velocity profile when the velocity in the boundary layer drops due to the larger viscous force's raised resistance. Figure 4 depicts a reduction in the velocity distribution for the Casson fluid parameter α. Because of the resistive force produced by tensile tension as a result of elasticity, the velocities show this decrease. In the simplest terms, as the Casson fluid parameter α rises, the yield stress and momentum boundary layer thickness drop. As values of it are increased, this results in narrower velocity distributions. A higher Casson fluid parameter causes the fluid to physically thicken. In other words, the Casson fluid is viewed as a fluid with variable plastic dynamic viscosity and a severe yield stress. For an increase in the values of the Casson fluid parameter, the velocity improves near the wall and barely

Table 5: Numerical data of Sherwood $ShRe^{-0.5}$.

Scenarios	Case 1	Case 2	Case 3	Case 4
1	0.1179952 26582382	0.0932262 818479224	0.0749832 964635284	0.06110907 50309176
2	0.117887 946298353	0.09322628 18479224	0.0736867 064590734	0.0580219 353888552
3	0.0932262 818479224	0.07808067 82255672	0.0655529 629746252	0.0550150 116690053
4	0.09822 36882754476	0.088517587 8738322	0.0798747 756202284	0.0721333 625772916
5	0.09322 62818479224	0.1349912 63204469	0.1704225 85875082	0.1954124 04593031
6	0.0932262 818479224	0.04414700 68737465	0.0096419 4790589059	-0.0173551 553821454
7	0.093226 2818479224	0.1304241 42760356	0.16791219 3587923	0.20568768 0106044
8	0.0932262 818479224	0.08722313 67226959	0.08248743 37826205	0.07858288 06943903
9	0.1225055 30397279	0.0932262 818479224	0.0694224 341590256	0.05809795 15113728
10	0.263658 247555587	0.1892008 10603047	0.0932262 818479224	-0.04074624 94958941
11	0.09322628 18479224	0.1136190 15821055	0.1318035 92190743	0.1480700 40769088
12	0.09322628 18479224	0.10191090 8954176	0.11059553 6059889	0.11928016 3165872
13	0.0932262 818479224	0.14931096 8798927	0.18967129 4660286	0.2194454 60126067
14	0.1179952 26582382	0.09322628 18479224	0.07498329 64635284	0.061109075 0309176
15	0.09322628 18479224	0.044147006 8737465	0.00964194 790589059	-0.01735515 53821454

Table 6: Comparison of results for the skin friction and local Nusselt number.

β	Ha	Ec	Pr	Sr	Sc	Kr	$Cf_x Re_x^{0.5}$ Ref. [10]	$Cf_x Re_x^{0.5}$ (new)	$-Nu_x Re_x^{-0.5}$ Ref. [10]	$-Nu_x Re_x^{-0.5}$ (new)
1.0	0.5	0.1	0.7	0.1	0.7	0.1	1.42514	1.42621	0.31172	0.30301
1.5							1.51744	1.51293	0.29046	0.29507
2.0							1.60514	1.60481	0.27206	0.26596
2.5							1.68877	1.67257	0.25595	0.25660

lowers far from the vertical heated wall. It has been noted that the current work and the work done by [17] are in good agreement. For porous parameterγ, the drag force and porosity parameter are closely related. Based on the result, the velocity drops when the porous parameter rises due to an increase in the quadratic drag. Figure 5 demonstrates that the velocity profile of heat and mass fluxes for the Casson-Maxwell fluid is zero near the wall. If you look at Figure 6, you will see that the temperature $\theta(\eta)$ becomes a declining function of the Prandtl number Pr. The ratio of thermal diffusivity to momentum diffusivity is known as the Prandtl number Pr. Raising Pr has been found to lower the temperature profile because it lowers the thermal diffusion rate, because increasing Pr implies that heat conduction is more significant than convection and that thermal diffusivity is predominate. According to this theory, the temperature decays because thermal diffusivity is less effective than momentum diffusivity in response to Pr. Due to the increased thermal state of the fluid in Figure 7 when in comparison with ambient fluid temperature, the temperature and thermal boundary layer thickness are boosted at a bigger temperature ratio θ_w. In Figure 8, the values of temperature $\theta(\eta)$ are increased with the increase of the Eckert number Ec, while having opposite behavior for thermal radiation Rd as seen in Figure 9. In Figure 10, the effect of the Schmidt number Sc upon the concentration profile $\phi(\eta)$ is indicated. Given that the kinematic viscosity(ν)and the Brownian diffusion coefficient(DB)are divided, it is observed that mass diffusion decreases following an increase inSclevels. The fluid's concentration falls as a result of this. As a result, $\phi(\eta)$, on boosting Sc, exhibits a deteriorating character. In Figure 11, the values of the concentration profile $\phi(\eta)$ were increased with the increase of chemical reaction parameter Kr, while having an opposite behavior for dimensionless rate constant m as seen in Figure 12. An analysis of the impact of the Soret number Sr on the concentration profile $\phi(\eta)$ is shown in Figure 13. The ratio of the temperature difference to concentration is called Sr. The temperature gradient increases as Sr increases. There is a perception of an increase in molecule diffusion. As a result, the rate of mass transfer accelerates for rising Sr values. As a result, $\phi(\eta)$ improves. Figure 14 discusses the appearance of rising activation energy E_1 values. It has been observed that increasing values of E_1 cause the Arrhenius function to degrade and the fluid concentration to fall. This is in line with the results of inclined practise applications since it uses the least amount of energy possible to initiate an activity [9]. For Figures 15 and 16, it is obvious that as Ha values grow, so does the rate of heat transfer and the temperature profile $\theta(\eta)$. The Lorentz forces appear to grow with greater Ha, which increases the opposing forces on the fluid particles and raises temperature. At higher temperature ratios θ_w, the concentration $\phi(\eta)$ and boundary layer thickness are also enhanced.

6. Conclusion

The importance of non-Newtonian fluid flows in numerous industrial and technical processes has made them a topic worth exploring in recent years. Examples of materials exhibiting non-Newtonian fluid characteristics include shampoos, soaps, muds, apple sauce, polymeric liquids, sugar solutions, condensed milk, tomato paste, paints, and blood at low shear rates. However, due to the diversity of their rheological properties, it is impossible to examine their behavior using a single constitutive correlation. Different fluid models have been developed as a result to precisely define the nature of non-Newtonian materials. Over a stretched sheet, we investigate the characteristics of a chemically reactive Casson-Maxwell fluid. Effects of activation energy are thought about. The following list summarizes the main points:

(i) As the Cassion fluid, magnetic, Maxwell fluid, and porosity parameters rise, the velocity field falls

(ii) Low temperature is associated with raising the thermal radiation parameter, while the Eckert number and temperature ratio both show a reversal trend

(iii) This model significantly improves the fluid's thermal performance when combined with the Arrhenius activation energy, magnetic field, Joule heating, and viscous dissipation

(iv) The effect of increasing Kr and θ_w is highly noticeable on the sheet's concentration distribution

(v) The study's findings presented here may be useful to both scientists and engineers who are conducting research as well as to individuals who are actively working in these fields

Symbols

τ_{ij}, P_y, and e_{ij}:	Cauchy stress tensor, yield stress of fluid, and deformation rate with components (x, y), respectively
μ_B, μ_0, and μ_∞:	Casson fluid plastic dynamics viscosity and limiting viscosity at zero shear rate and at infinite shear rate, respectively
λ, μ, and ρ:	The relaxation time, viscosity, and density, respectively
T_w, C_w, T_∞, and C_∞:	Wall temperature and concentration, respectively, and free stream temperature and concentration, respectively
σ, B_o, and k:	Electrical conductivity, intensity of the external magnetic field, and permeability, respectively
c_p, q_r, and K_T:	Specific heat, radiative heat flux, and thermal-diffusion ratio, respectively
D_N, σ^*, and $K_{r'}$:	The diffusion parameter, Stefan-Boltzmann constant, and chemical reaction coefficient, respectively
T_m, k^*, and K:	The mean temperature, mean absorption coefficient, and thermal conductivity, respectively
a, γ, and E^*:	Positive constant, porosity parameter, and activation energy, respectively
M, β, and α:	The magnetic, Maxwell, and Casson parameters, respectively
Pr, Ec, and Sc:	Prandtl, Eckert, and Schmidt numbers, respectively
Kr, Rd, and m:	Chemical reaction, thermal radiation parameters, and dimensionless rate constant, respectively
Sr and θ_w:	Soret number and temperature ratio parameter, respectively.

Data Availability

Data available upon request.

Additional Points

Highlights. (i) Applying Arrhenius activation energy on MHD chemically reactive Casson-Maxwell fluid over a stretched sheet. (ii) To achieve the required solution of the problem, an innovative work of Lobatto IIIA methodology via MATLAB software is used. (iii) Data visualizations and numerical examples are presented considering the many physical restrictions.

Conflicts of Interest

The author declares that they have no conflicts of interest to report regarding the present study.

Acknowledgments

The researcher would like to acknowledge the Deanship of Scientific Research, Taif University, for this work.

References

[1] M. Saqib, H. Hanif, T. Abdeljawad, I. Khan, S. Shafie, and K. Sooppy Nisar, "Heat transfer in MHD flow of Maxwell fluid via fractional Cattaneo-Friedrich model: a finite difference approach," *Computers, Materials & Continua*, vol. 65, no. 3, pp. 1959–1973, 2020.

[2] F. S. Bayones, A. M. Abd-Alla, and E. N. Thabet, "Magnetized dissipative Soret effect on nonlinear radiative Maxwell nanofluid flow with porosity, chemical reaction and Joule heating," *Waves in Random and Complex Media*, pp. 1–19, 2022.

[3] S. A. Shehzad, M. G. Reddy, A. Rauf, T. Mushtaq, and F. M. Abbasi, "Magnetohydrodynamic squeezing micropolar nanofluid flow confined in parallel disks with implication of Maxwell-Cattaneo law," *Physica Scripta*, vol. 98, no. 6, article 065201, 2023.

[4] C. Christov, "On frame indifferent formulation of the Maxwell-Cattaneo model of finite-speed heat conduction," *Mechanics Research Communications*, vol. 36, no. 4, pp. 481–486, 2009.

[5] F. S. Bayones, A. M. Abd-Alla, and E. N. Thabet, "Effect of heat and mass transfer and magnetic field on peristaltic flow of a fractional Maxwell fluid in a tube," *Complexity*, vol. 2021, Article ID 9911820, 12 pages, 2021.

[6] C. Liu, M. U. Khan, M. Ramzan et al., "Nonlinear radiative Maxwell nanofluid flow in a Darcy–Forchheimer permeable media over a stretching cylinder with chemical reaction and bioconvection," *Scientific Reports*, vol. 11, no. 1, p. 9391, 2021.

[7] K. Sudarmozhi, D. Iranian, I. Khan, J. Alzahrani, A. S. Aljohani, and S. M. Eldin, "Double diffusion in a porous medium of MHD Maxwell fluid with thermal radiation, heat generation and chemical reaction," *Case Studies in Thermal Engineering*, vol. 43, article 102700, 2023.

[8] A. S. Kotnurkar, N. Kallolikar, and E. N. Thabet, "Double-diffusive bioconvection effects on multi-slip peristaltic flow of Jeffrey nanofluid in an asymmetric channel," *Pramana*, vol. 97, no. 3, 2023.

[9] M. I. Ur Rehman, H. Chen, W. Jamshed, M. R. Eid, K. Guedri, and S. M. El Din, "Thermal radiative flux and energy of Arrhenius evaluation on stagnating point flowing of Carreau nanofluid: a thermal case study," *Case Studies in Thermal Engineering*, vol. 40, article 102583, 2022.

[10] S. Suraiah Palaiah, H. Basha, G. J. Reddy, and M. A. Sheremet, "Magnetized dissipative Soret effect on chemically reactive Maxwell fluid over a stretching sheet with Joule heating," *Coatings*, vol. 11, no. 5, p. 528, 2021.

[11] A. M. Abd-Alla, E. N. Thabet, F. S. Bayones, and A. M. Alsharif, "Heat transfer in a non-uniform channel on MHD peristaltic flow of a fractional Jeffrey model via porous medium," *Indian Journal of Physics*, vol. 97, no. 6, pp. 1799–1809, 2023.

[12] A. M. Abd-Alla, S. M. Abo-Dahab, E. N. Thabet, and M. A. Abdelhafez, "Heat and mass transfer for MHD peristaltic flow in a micropolar nanofluid: mathematical model with thermophysical features," *Scientific Reports*, vol. 12, no. 1, article 21540, 2022.

[13] R. S. Varun Kumar, P. Gunderi Dhananjaya, R. Naveen Kumar, R. J. Punith Gowda, and B. C. Prasannakumara, "Modeling and theoretical investigation on Casson nanofluid flow over a curved stretching surface with the influence of magnetic field and chemical reaction," *International Journal for Computational Methods in Engineering Science and Mechanics*, vol. 23, no. 1, pp. 12–19, 2022.

[14] M. Tamoor, M. Waqas, M. I. Khan, A. Alsaedi, and T. Hayat, "Magnetohydrodynamic flow of Casson fluid over a stretching cylinder," *Results in Physics*, vol. 7, pp. 498–502, 2017.

[15] S. Ghadikolaei, K. Hosseinzadeh, D. Ganji, and B. Jafari, "Nonlinear thermal radiation effect on magneto Casson nanofluid flow with Joule heating effect over an inclined porous stretching sheet," *Case Studies in Thermal Engineering*, vol. 12, pp. 176–187, 2018.

[16] M. Sohail, Z. Shah, A. Tassaddiq, P. Kumam, and P. Roy, "Entropy generation in MHD Casson fluid flow with variable heat conductance and thermal conductivity over non-linear bi-directional stretching surface," *Scientific Reports*, vol. 10, no. 1, article 12530, 2020.

[17] M. Sohail, H. Alrabaiah, U. Ali, F. T. Zohra, M. M. Selim, and P. Thounthong, "Numerical exploration of thermal and mass transportation by utilising non-Fourier double diffusion theories for Casson model under Hall and ion slip effects," *Pramana*, vol. 95, no. 4, 2021.

[18] P. B. Raafat and F. N. Ibrahim, "Entropy and heat transfer investigation of Casson–Maxwell, Casson–Jeffrey, and Casson–Oldroyd-B binary nanofluids in a parabolic trough solar collector: a comparative study," *Journal of Thermal Analysis and Calorimetry*, vol. 148, no. 10, pp. 4477–4493, 2023.

[19] N. Kanimozhi, R. Vijayaragavan, and B. Rushi Kumar, "Impacts of multiple slip on magnetohydrodynamic Williamson and Maxwell nanofluid over a stretching sheet saturated in a porous medium," *Numerical Heat Transfer, Part B: Fundamentals*, pp. 1–17, 2023.

[20] K. Gangadhar, E. Mary Victoria, K. Bhanu Lakshmi, and A. J. Chamkha, "Nonlinear radiation phenomena for Casson–Maxwell nanoliquid flow with chemical reactions," *Proceedings of the Institution of Mechanical Engineers, Part E: Journal of Process Mechanical Engineering*, vol. 237, no. 6, pp. 2123–2133, 2023.

[21] J. K. Madhukesh, G. K. Ramesh, S. A. Shehzad, S. Chapi, and I. Prabhu Kushalappa, "Thermal transport of MHD Casson–Maxwell nanofluid between two porous disks with Cattaneo–Christov theory," *Numerical Heat Transfer, Part A: Applications*, pp. 1–16, 2023.

[22] R. J. P. Gowda, A. Rauf, R. Naveen Kumar, B. C. Prasannakumara, and S. A. Shehzad, "Slip flow of Casson–Maxwell nanofluid confined through stretchable disks," *Indian Journal of Physics*, vol. 96, no. 7, pp. 2041–2049, 2022.

[23] J. Cui, U. Farooq, A. Jan et al., "Significance of nonsimilar numerical simulations in forced convection from stretching cylinder subjected to external magnetized flow of Sisko fluid," *Journal of Mathematics*, vol. 2021, Article ID 9540195, 11 pages, 2021.

[24] J. Cui, R. Razzaq, F. Azam, U. Farooq, M. Hussain, and A. J. Chamkha, "Nonsimilar forced convection analysis of

chemically reactive magnetized Eyring-Powell nanofluid flow in a porous medium over a stretched Riga surface," *Journal of Porous Media*, vol. 25, no. 10, pp. 67–81, 2022.

[25] A. Jan, M. Mushtaq, U. Farooq, and M. Hussain, "Nonsimilar analysis of magnetized Sisko nanofluid flow subjected to heat generation/absorption and viscous dissipation," *Journal of Magnetism and Magnetic Materials*, vol. 564, article 170153, 2022.

[26] J. Cui, A. Jan, U. Farooq, M. Hussain, and W. A. Khan, "Thermal analysis of radiative Darcy–Forchheimer nanofluid flow across an inclined stretching surface," *Nanomaterials*, vol. 12, no. 23, p. 4291, 2022.

[27] M. Hussain, J. Cui, U. Farooq, M. E. A. Rabie, and T. Muhammad, "Nonsimilar modeling and numerical simulations of electromagnetic radiative flow of nanofluid with entropy generation," *Mathematical Problems in Engineering*, vol. 2022, Article ID 4272566, 20 pages, 2022.

[28] S. Riaz, M. F. Afzaal, Z. Wang, A. Jan, and U. Farooq, "Numerical heat transfer of non-similar ternary hybrid nanofluid flow over linearly stretching surface," *Numerical Heat Transfer, Part A: Applications*, pp. 1–15, 2023.

[29] A. M. Jyothi, R. Naveen Kumar, R. J. Punith Gowda, Y. Veeranna, and B. C. Prasannakumara, "Impact of activation energy and gyrotactic microorganisms on flow of Casson hybrid nanofluid over a rotating moving disk," *Heat Transfer*, vol. 50, no. 6, pp. 5380–5399, 2021.

[30] N. N. Kumar, D. R. Sastry, and S. Shaw, "Irreversibility analysis of an unsteady micropolar CNT-blood nanofluid flow through a squeezing channel with activation energy-application in drug delivery," *Computer Methods and Programs in Biomedicine*, vol. 226, article 107156, 2022.

[31] C. Sowmiya and B. Rushi Kumar, "MHD Maxwell nanofluid flow over a stretching cylinder in porous media with microorganisms and activation energy," *Journal of Magnetism and Magnetic Materials*, vol. 582, article 171032, 2023.

[32] M. Khan, T. Salahuddin, M. M. Yousaf, F. Khan, and A. Hussain, "Variable diffusion and conductivity change in 3D rotating Williamson fluid flow along with magnetic field and activation energy," *International Journal of Numerical Methods for Heat and Fluid Flow*, vol. 30, no. 5, pp. 2467–2484, 2020.

[33] P. Kumar, H. Poonia, S. Areekara, A. S. Sabu, A. Mathew, and L. Ali, "Significance of irregular heat source and Arrhenius energy on electro-magnetohydrodynamic hybrid nanofluid flow over a rotating stretchable disk with nonlinear radiation," *Numerical Heat Transfer, Part A: Applications*, pp. 1–23, 2023.

[34] M. R. Khan, A. S. Al-Johani, A. M. Elsiddieg, T. Saeed, and A. A. A. Mousa, "The computational study of heat transfer and friction drag in an unsteady MHD radiated Casson fluid flow across a stretching/shrinking surface," *International Communications in Heat and Mass Transfer*, vol. 130, article 105832, 2022.

[35] A. A. Dar, "Effect of thermal radiation, temperature jump and inclined magnetic field on the peristaltic transport of blood flow in an asymmetric channel with variable viscosity and heat absorption/generation," *Iranian Journal of Science and Technology, Transactions of Mechanical Engineering*, vol. 45, no. 2, pp. 487–501, 2021.

[36] C. M. Mohana and B. R. Kumar, "Nanoparticle shape effects on hydromagnetic flow of Cu-water nanofluid over a nonlinear stretching sheet in a porous medium with heat source, thermal radiation, and Joule heating," *ZAMM-Journal of Applied Mathematics and Mechanics/Zeitschrift f¨Ur Angewandte Mathematik Und Mechanik*, 2023.

[37] K. Padmaja, B. R. Kumar, O. A. Bég, and T. A. Bég, "Cross-diffusion and higher-order chemical reaction effects on hydromagnetic copper-water nanofluid flow over a rotating cone in a porous medium," *Journal of Multiscale Modelling*, vol. 14, no. 3, pp. 2350006–2350585, 2023.

[38] A. M. Abd-Alla, S. M. Abo-Dahab, E. N. Thabet, and M. A. Abdelhafez, "Impact of inclined magnetic field on peristaltic flow of blood fluid in an inclined asymmetric channel in the presence of heat and mass transfer," *Waves in Random and Complex Media*, pp. 1–25, 2022.

[39] A. M. Abd-Alla, S. M. Abo-Dahab, E. N. Thabet, and M. A. Abdelhafez, "Peristaltic pump with heat and mass transfer of a fractional second grade fluid through porous medium inside a tube," *Scientific Reports*, vol. 12, no. 1, article 10608, 2022.

[40] T. Muhammad, A. Alsaedi, T. Hayat, and S. A. Shehzad, "A revised model for Darcy-Forchheimer three-dimensional flow of nanofluid subject to convective boundary condition," *Results in Physics*, vol. 7, pp. 2791–2797, 2017.

[41] M. Hassan, M. Marin, A. Alsharif, and R. Ellahi, "Convective heat transfer flow of nanofluid in a porous medium over wavy surface," *Physics Letters A*, vol. 382, no. 38, pp. 2749–2753, 2018.

[42] M. Bhatti, A. Zeeshan, R. Ellahi, and G. Shit, "Mathematical modeling of heat and mass transfer effects on MHD peristaltic propulsion of two-phase flow through a Darcy-Brinkman-Forchheimer porous medium," *Advanced Powder Technology*, vol. 29, no. 5, pp. 1189–1197, 2018.

[43] K. Padmaja and R. Kumar, "Higher order chemical reaction effects on Cu–H_2O nanofluid flow over a vertical plate," *Scientific Reports*, vol. 12, no. 1, article 17000, 2022.

[44] A. M. Abd-Alla, E. N. Thabet, and F. S. Bayones, "Numerical solution for MHD peristaltic transport in an inclined nanofluid symmetric channel with porous medium," *Scientific Reports*, vol. 12, no. 1, p. 3348, 2022.

[45] B. Sharma and R. Gandhi, "Combined effects of Joule heating and nonuniform heat source/sink on unsteady MHD mixed convective flow over a vertical stretching surface embedded in a Darcy-Forchheimer porous medium," *Propulsion and Power Research*, vol. 11, no. 2, pp. 276–292, 2022.

[46] A. Abd-Alla, S. Abo-Dahab, E. N. Thabet, F. Bayones, and M. Abdelhafez, "Heat and mass transfer in a peristaltic rotating frame Jeffrey fluid via porous medium with chemical reaction and wall properties," *Alexandria Engineering Journal*, vol. 66, pp. 405–420, 2022.

[47] M. E. Ghoneim, Z. Khan, S. Zuhra, A. Ali, and E. Tag-Eldin, "Numerical solution of Rosseland's radiative and magnetic field effects for Cu-kerosene and Cu-water nanofluids of Darcy-Forchheimer flow through squeezing motion," *Alexandria Engineering Journal*, vol. 64, pp. 191–204, 2023.

[48] A. Paul and T. K. Das, "Darcy–Forchheimer MHD radiative flow through a porous space incorporating viscous dissipation, heat source, and chemical reaction effect across an exponentially stretched surface," *Heat Transfer*, vol. 52, no. 1, pp. 807–825, 2023.

[49] E. N. Thabet, Z. Khan, A. M. Abd-Alla, and F. S. Bayones, "Thermal enhancement, thermophoretic diffusion, and Brownian motion impacts on MHD micropolar nanofluid over an

inclined surface: numerical simulation," *Numerical Heat Transfer, Part A: Applications*, pp. 1–20, 2023.

[50] N. Hafez, E. N. Thabet, Z. Khan, A. Abd-Alla, and S. Elhag, "Electroosmosis-modulated Darcy Forchheimer flow of Casson nanofluid over stretching sheets in the presence of Newtonian heating," *Case Studies in Thermal Engineering*, vol. 53, article 103806, 2024.